Counihan *et al. Energy Mater.* **2025**, *5*, 500032
DOI: 10.20517/energymater.2024.195

Energy Materials

Article

Open Access

Check for updates

Improved interfacial li-ion transport in composite polymer electrolytes via surface modification of LLZO

Michael J. Counihan[1], Jungkuk Lee[2], Priyadarshini Mirmira[3], Pallab Barai[2], Meghan E. Burns[1,4], Chibueze V. Amanchukwu[3], Venkat Srinivasan[5], Yuepeng Zhang[2], Sanja Tepavcevic[1,*]

[1]Materials Science Division, Argonne National Laboratory, Lemont, IL 60439, USA.
[2]Applied Materials Division, Argonne National Laboratory, Lemont, IL 60439, USA.
[3]Pritzker School of Molecular Engineering, University of Chicago, Chicago, IL 60637, USA.
[4]Department of Chemistry, University of Chicago, Chicago, IL 60637, USA.
[5]Chemical Sciences and Engineering Division, Argonne National Laboratory, Lemont, IL 60439, USA.

[*]**Correspondence to:** Dr. Sanja Tepavcevic, Materials Science Division, Argonne National Laboratory, 9700 S Cass Ave, Lemont, IL 60439, USA. E-mail: sanja@anl.gov

How to cite this article: Counihan, M. J.; Lee, J.; Mirmira, P.; Barai, P.; Burns, M. E.; Amanchukwu, C. V.; Srinivasan, V.; Zhang, Y.; Tepavcevic, S. Improved interfacial li-ion transport in composite polymer electrolytes via surface modification of LLZO. *Energy Mater.* **2025**, *5*, 500032. https://dx.doi.org/10.20517/energymater.2024.195

Received: 28 Sep 2024 **First Decision:** 31 Oct 2024 **Revised:** 21 Nov 2024 **Accepted:** 30 Nov 2024 **Published:** 23 Jan 2025

Academic Editors: Jinping Liu, Jiaqi Huang **Copy Editor:** Ping Zhang **Production Editor:** Ping Zhang

Abstract

Composite polymer electrolytes that incorporate ceramic fillers in a polymer matrix offer mechanical strength and flexibility as solid electrolytes for lithium metal batteries. However, fast Li^+ transport between polymer and Li^+-conductive filler phases is not a simple achievement due to high barriers for Li^+ exchange across the interphase. This study demonstrates how modification of $Li_7La_3Zr_2O_{12}$ (LLZO) nanofiller surfaces with silane chemistries influences Li^+ transport at local and global electrolyte scales. Anhydrous reactions covalently link amine-functionalized silanes [(3-aminopropyl)triethoxysilane (APTES)] to LLZO nanoparticles, which protects LLZO in air. APTES functionalization lowers the poly (ethylene oxide) (PEO)-LLZO interphase resistance to half that of unmodified LLZO and increases effective Li^+ transference number, while insulating Al_2O_3 completely blocks ion exchange and lowers transference number and conductivity in PEO-lithium bis(trifluoromethanesulfonyl)imide (LiTFSI)-LLZO composites. Modeling an inner resistive interphase between LLZO and PEO surrounded by an outer conductive interphase explains non-linear conductivity trends. Solid-state ^7Li & ^6Li nuclear magnetic resonance shows Li^+ only exchanges between PEO-LiTFSI and some LLZO interphase, with no appreciable Li^+ transport through bulk LLZO. Surface functionalization is a promising path toward lowering the polymer-ceramic interphase resistance. This work demonstrates that local changes in Li^+ transport affect macroscopic performance, highlighting

the intricate relationships between all interfaces in inherently heterogeneous composite polymer electrolytes.

Keywords: Composite polymer electrolyte, LLZO, interface, interphase, silane, lithium vacancies, ion transport

INTRODUCTION

Composite polymer electrolytes (CPEs) are a promising candidate for solid-state lithium metal batteries that require strong yet flexible electrolytes[1-3]. While the polymer matrix ensures this flexibility and good electrode contact, ceramic fillers add mechanical strength[4-6]. Adding active fillers - those that transport lithium ions through ceramic phase - can possibly increase total lithium ion conductivity[2], enabling fast charging rates for various applications such as electric vehicles. However, with common fillers such as $Li_7La_3Zr_2O_{12}$ (LLZO) nanoparticles (NPs) and nanofibers (NFs), increasing conductivity and Li^+ transference number (t_{Li+}) (the current fraction carried by Li^+) are not easily attained by simply mixing the nanofillers into a lithium-salt-containing polymer matrix. Several researchers have reported decreases in CPE conductivity with increasing weight fractions of LLZO of various morphologies[7-11]. While many studies claim increases in Li^+ conductivity with different mixtures of LLZO, polymer, and other additives, the evidence for direct Li^+ transport from the polymer phase through the LLZO phase is dubious. In-depth research on LLZO-polymer composites has shown fundamental, physical-chemical limits to Li^+ exchange at the ceramic-polymer interface, whether due to polymer and ion dynamics[12,13] or reacted surface layers on the LLZO[14].

To overcome this large barrier to Li^+ exchange between Li^+-conducting fillers and the polymer matrix, recent research has focused on functionalization of the filler surface. The most common modification is via silane chemistry[15-19], a relatively simple way to covalently bond some functional organic chemistry to the oxide particle surface via Si-O bonds. Ideally, bridging the gap between organic polymer and inorganic filler phases with the silane will activate the bulk of the active filler (or at least the filler surface) for Li^+ transport. While this approach seems successful with sulfide active fillers[15,19], functionalizing LLZO and other oxide fillers does not boost conductivity of the composite up to even one order of magnitude higher than the unfunctionalized material or polymer matrix alone at optimum filler loadings[16-18]. Thus, there appears to still be some fundamental barrier for activating "bulk-to-bulk" LLZO-to-polymer Li^+ transport, either due to slow microscopic Li^+ exchange at the LLZO surface and/or a macroscopic resistance accumulated over numerous interfacial Li^+ exchanges to transport Li^+ through the composite[20]. Moreover, even if bulk conductivity can be significantly increased by activating the active fillers, most of the battery resistance at the lab scale comes from the lithium anode-electrolyte interface. This is mostly attributed to resistance to Li^+ transport across the solid-electrolyte interphase (SEI) and is apparent from virtually all impedance data in the composite electrolyte literature[10]. Whether or not filler surface modification impacts this interface resistance remains an open question, but one worth answering so that area-specific resistance can be minimized for optimal battery efficiency.

Herein, we studied the effect of silane modification of LLZO NPs and NFs on multiple chemical and electrochemical characteristics in CPEs. An anhydrous synthesis procedure allows attachment of amine [(3-aminopropyl)triethoxysilane (APTES)] and epoxy [(3-glycidyloxypropyl)trimethoxysilane (GPS)] functionalities to LLZO without exposure to air, which minimizes surface lithium carbonate formation and disruption of the bulk LLZO structure by H^+/Li^+ exchange. At 10 wt % LLZO NPs loading in a poly (ethylene oxide)-lithium bis(trifluoromethanesulfonyl)imide (PEO-LiTFSI) matrix, there is no effect of LLZO surface chemistry, as CPEs with unmodified, APTES-modified, and Al_2O_3-coated LLZO all have identical conductivities slightly higher than PEO-LiTFSI alone. At 50 wt % LLZO, the surface chemistry

dominates ion transport, with Al_2O_3-modified LLZO composites decreasing conductivity more than an order of magnitude versus other samples, while APTES-modified LLZO composites show a slight decrease in conductivity relative to unmodified LLZO but the highest effective t_{Li+}. This is due to a ca. 50% decrease in PEO-LLZO interphase resistance with the APTES coating, as quantified by impedance measurements with defined geometry PEO-LITFSI|LLZO|PEO-LiTFSI electrolytes. The trend of local conductivity maximum and the effect of surface functionality is analyzed with a two-interphase model, where a conductive interphase forms around LLZO as it plasticizes the PEO but a resistive interphase forms on the LLZO surface due to different polymer dynamics at the (functionalized) LLZO surface. The variation in composite conductivity with LLZO fraction is well captured by the proposed two-interphase model, which is a major finding reported in this manuscript.

Solid-state ^{7}Li and ^{6}Li nuclear magnetic resonance (NMR) shows that Li^+ only exchanges between the PEO-LiTFSI phase and a LLZO interphase, with virtually no Li^+ transport through the bulk LLZO. The second major finding of this article is the demonstration of a mechanism where Li^+ transports exclusively along and not through the LLZO-PEO interface, which is aided by APTES functionalization. Finally, we also show the indirect connections between locally high Li^+ transport at the LLZO surface and global cell characteristics such as critical current density and anode interface resistance. This study presents new ways to functionalize and utilize ceramic fillers for composite electrolytes while shedding light on the transport processes physically and chemically.

EXPERIMENTAL

Materials

PEO (M_v~600 kDa), LiTFSI (99.95% metals basis), acetonitrile (ACN, 99.8%, anhydrous), APTES (98%), GPS (98%), toluene (99.8%, anhydrous), lithium nitrate ($LiNO_3$), lanthanum(III) nitrate hydrate [$La(NO_3)_3$•xH_2O], zirconium(IV) oxynitrate hydrate [$ZrO(NO_3)_2$•xH_2O], aluminum nitrate nonahydrate [$Al(NO_3)_3$•$9H_2O$], and dimethylformamide (DMF) were purchased from Sigma-Aldrich. Methanol (MeOH, HPLC grade), acetic acid (AcOH, glacial, Certified ACS), and polyvinylpyrrolidone (PVP, average MW = 1.3 MDa) were purchased from Fisher Scientific. Millipore water was used as a pure water source. Al-doped LLZO NPs (nominal composition of $Li_{6.25}Al_{0.25}La_3Zr_2O_{12}$) with a size of D_{50} = 500 nm were from Ampcera. Al-doped LLZO NFs with the same composition and 200-300 nm diameter were prepared via electrospinning and annealing according to our previous work[10]. The chemical composition of LLZO NPs and LLZO NFs was characterized by inductively coupled plasma optical emission spectroscopy (ICP-OES, Agilent 5110) [Supplementary Table 1]. Ta-doped LLZO sintered pellets prepared via solid-state reaction[21] were generously provided by Dr. Chih-Long Tsai. Ionic conductivity of Ta-doped LLZO pellets was 5.87 10^{-4} S cm^{-1} and electronic conductivity is 5.11 × 10^{-10} S cm^{-1} at 25 °C, with the Li-ion transfer number 0.9976. N_2 absorption Brunauer-Emmett-Teller (BET) and Krypton BET measurements did not give any result due to the very low surface area of the pellets, even though we used many pellets to fill up the experimental glass container. For the relative density, by Archimedes' method, we measured theoretical density 5.35 g cm^{-3}, relative density 91.6% ± 0.4%, open porosity 0.2% ± 0.15% and close porosity 8.2% ± 0.16%.

Lithium foil electrodes [Li, 250 μm thickness, Micro Technology Innovation Korea (MTI Korea)] were polished with a steel brush and lint-free cloth to remove surface contaminants. Au@Cu electrodes were prepared by first cleaning 1.0 cm^2 copper foil (Cu, 6 μm thick, MSE Supplies) discs with dilute HCl and acetone, followed by sputtering 20 nm of gold at a rate of 1.0 Å/s (DST1-170 sputter coater, Element Pi). Isotopically enriched ^{6}Li metal (95 atom %, Sigma-Aldrich) was cut and pressed between steel plates before polishing, followed by typical cell assembly with electrode areas of 0.7-1.0 cm^2.

Composite electrolytes

CPEs with 0, 10 and 50 wt % LLZO NPs were prepared by mixing PEO, LiTFSI, and LLZO NPs in acetonitrile. Briefly, LiTFSI and LLZO were first mixed by ultrasonication for 30 min, and then PEO was added into the solution followed by 30 min mixing with a dual-asymmetric centrifuge speed mixer (FlackTek SpeedMixer®). The PEO concentration was kept at 6 wt % (EO:Li ratio = 15:1), and the LLZO mass ratio was respected to that of PEO. After preparation, the viscous slurry was coated onto a polytetrafluoroethylene (PTFE) film (McMaster-Carr) via slot-die coating (FOM vectorSC, FOM Technology) and dried in ambient to yield homogeneous membranes of 50-60 μm thickness with ±2 μm variation in thickness across the membrane. Good ductility and relatively uniform fiber distribution in the polymer matrix were observed for these membranes [Supplementary Figure 1]. The authors also found that thinner membranes with a desired thickness of less than 20 μm and uniform fiber distribution can be obtained by optimizing slurry ink rheological properties and coating conditions such as slurry injection rate, coating gap, and web moving speed. The dry membranes were punched into 1.6 cm^2 area discs and into a glovebox for cell assembly. PEO-LiTFSI samples (0 wt % LLZO NP) were processed in an identical process but did not include LLZO nanomaterials.

For silane modification, LLZO was thermally treated at 620 °C for 30 min in argon to remove surface carbonates. Silane modification of LLZO was carried out by dispersing 1 g of LLZO NPs or 0.1 g of LLZO NFs in 80 mL toluene in a round-bottom flask inside the glovebox. After adding 3 ml of APTES or GPS, the mixture was stirred and refluxed under nitrogen for 24 h. The functionalized particles were centrifuged and washed with ethanol several times before drying to remove excess silane reagent. For the preparation of Al_2O_3-coated LLZO NPs, atomic layer deposition (ALD) of Al_2O_3 on LLZO NPs was performed in accordance with our previous work[10] for a Al_2O_3 thickness of ~10 nm. LLZO samples are noted as Neat LLZO, APTES@LLZO, GPS@LLZO, and Al_2O_3 for unmodified, APTES-functionalized, GPS-functionalized, and Al_2O_3-coated LLZO materials, respectively.

Electrochemical measurements

All electrochemical measurements were performed on a Biologic VSP300 potentiostat in a temperature-controlled chamber (ESPEC). Composite electrolytes were sandwiched between 0.9 cm^2 Li foil electrodes that were freshly polished. These were then assembled in 2032 coin cells with a 1.0 mm stainless steel spacer and wave spring; all cell parts were 304 stainless steel. Experiments were performed in triplicate with three cells of each composite electrolyte.

For trilayer electrolyte measurements, Ta-doped LLZO pellets were annealed in a muffle furnace inside an Ar-filled glovebox to remove surface contaminants[22-24]. The samples were placed in a MgO crucible with a lid and heated at 250 °C then 500 °C, with 5 °C/min ramps and one hour dwells each step before cooling naturally overnight. For APTES@LLZO pellets, the annealed LLZO was soaked in a 3 wt % solution of APTES in ACN inside the glovebox for several hours to mitigate any air exposure from the procedure required for LLZO NP functionalization, then rinsed thoroughly with ACN and dried. While this method differs from LLZO NP functionalization, it is still suitable for functionalization of the flat pellet surface compared to the more rigorous, longer reflux in toluene needed for high surface area NPs. After surface preparation, PEO-LiTFSI was drop-cast from a dilute ACN solution onto one side of the pellet, dried at 60 °C under vacuum for 30 min, and the same was repeated on the other pellet side. The total electrolyte thickness was measured after each drying step to determine PEO-LiTFSI thickness. Coin cells with 20 nm Au@Cu electrodes were prepared as above with a 0.5 mm spacer.

Cells were ramped from 5 to 70 °C at 5° C increments every 30 minutes, then ramped down and allowed to equilibrate at 60 °C before subsequent measurements. Electrochemical impedance (EIS) measurements were performed with a 7 MHz-1 or 0.1 Hz frequency range, 0.0 V *vs.* open circuit DC bias, 10 mV amplitude AC sine wave, and 20 points per decade sampling. Chronoamperometry was performed at +50 mV bias for 1,000 s with 1 mV/1 s sampling intervals to capture accurate currents. Galvanostatic cycling was performed in 10 μA/cm^2, 10 min steps with 40 min total rest time and EIS measurements in between each step. Transference numbers were estimated as the Bruce-Vincent current fraction[25]:

$$\rho_{BV} = \frac{i_{ss}}{i_0} \frac{(\Delta V - i_0 R_{Anode-Int,0})}{(\Delta V - i_{ss} R_{Anode-Int,ss})} \quad (1)$$

where i_0 and i_{ss} are the initial and steady-state currents from chronoamperometry, ΔV is the applied bias, and $R_{\text{Anode-Int,0/ss}}$ is the medium frequency resistance from EIS measurements before and after chronoamperometry. The apparent Arrhenius activation energy was determined for narrow temperature ranges via:

$$\sigma(T) = \sigma_0 \times exp\left(\frac{-E_a}{RT}\right) \quad (2)$$

where σ is the calculated conductivity from impedance measurements, E_a is the Arrhenius activation energy, R is the gas constant, and T is temperature.

Materials characterization

Fourier transform infrared spectroscopy (FT-IR) was performed using a Bruker Vertex 70 with an Attenuated Total Reflection (ATR) accessory. Raman microscopy was performed on a Renishaw inVia system with 633 nm laser at 5 mW and a 50x objective (NA = 0.5).

Solid-state NMR spectroscopy was performed on a Bruker Avance III wide-bore 400 MHz spectrometer under a field of 9.5 T. Samples were packed into a 1.9 mm ZrO_2 rotor with polyimide caps. All spectra were acquired while spinning at 20 kHz. ^{7}Li 1D spectra were acquired using the Larmor frequency of 155.5 MHz and a 90° pulse time of 0.9 μs with a corresponding power level of 90 W. Recycle delay times were optimized for each sample and varied between 20 - 40 s. ^{6}Li 1D spectra were acquired using the Larmor frequency of 58.9 MHz and a 90° pulse time of 5 μs at 40 W. The recycle delay time was fixed to 50 s. All $^{6/7}$Li chemical shifts were referenced to solid LiF at -1.0 ppm. 2D ^{7}Li-^{7}Li exchange were acquired using the same 90° pulse times as the 1D spectra. Additionally, 2D spectra were acquired using a recycle delay time of 3 s and a mixing time of 1.5 s.

Composite electrolyte samples were prepared for solid-state NMR with bidirectional galvanostatic cycling at 5-10 μA for 5-7 days with ^{6}Li foil electrodes at room temperature. The cell was disassembled, the electrodes were removed, and any excess pieces of lithium metal were cut from the sample with a razor blade since residual metal can disrupt the magic-angle spinning. The ^{6}Li-enriched samples were then loaded into 1.9 mm ZrO_2 rotors in ambient atmosphere; exposure to ambient is not expected to influence the distribution of Li^+ in the sample.

Modeling

A detailed description of the computational model for estimating conductivity and transference number can be found in the Supplementary Materials.

RESULTS AND DISCUSSION

Surface modification and stability of LLZO nanofillers

LLZO NPs and NFs (nanofillers generally) were modified via silane chemistry. Silane modification allows the covalent attachment of many pendant groups to the oxide surface, where these chemistries can increase the interaction with the surrounding polymer matrix to influence local Li^+ transport. Since LLZO is very sensitive to humid air, we developed an anhydrous toluene-based synthesis procedure. LLZO nanofillers (1 g) were dispersed in 80 mL of toluene in an Ar-filled glovebox. The APTES silane reagent was then added to the mixture, which was stirred under reflux and nitrogen for 24 h. When a short reflux time was used (e.g., 4 h), Raman shifts confirmed that ATPES amount was not sufficient to protect LLZO from ambient exposure [Figure 1A and B]. The particles were then centrifuged and washed repeatedly to remove excess silane before final isolation and drying. The chemical composition of APTES-modified LLZO was characterized by ICP-OES [Supplementary Table 1]. Compared to the neat LLZO NP (Li = 5.99), the ATPES-modified LLZO NP shows slightly lower Li content (Li = 4.68), indicating loss of Li during the surface modification.

Figure 1C shows FT-IR spectra of unmodified LLZO NPs ("Neat LLZO NP") and LLZO NPs treated with an amine-terminated silane APTES ("APTES@LLZO NP"), showing clear emergence of peaks related to the silane (1,575 and 3,550 cm^{-1} for N-H stretching) and attenuation of peaks (3,675 cm^{-1} for O-H stretching) related to common LLZO surface contaminants. These changes are more apparent with differential absorbance [Figure 1D], where the appearance of N-H, C-H, and Si-O-Si bond vibrations show the APTES is successfully attached to the LLZO surface. Interestingly, there is also a loss of O-H and O_2C-O vibrations from LiOH and Li_2CO_3, respectively. This indicates that the treatment removed some (but still not all) of the native LLZO surface contaminant layer, something unexpected for a non-acidic, simplistic non-aqueous treatment[26-29]. It is also possible that LiOH and Li_2CO_3 were prevented from forming further when the sample was exposed to air for the measurement.

This last observation reveals another benefit of silane modification of LLZO - the ability to process the electrolytes in air. To highlight this, we performed in situ Raman spectroscopy on LLZO NFs. The NFs have the same nominal chemical composition as the commercial NPs but have much higher surface area. This greater area increases the rate of reaction with humid air, leading to the formation of LiOH, which then reacts with CO_2 to form a Li_2CO_3 surface layer. Meanwhile, Li^+ ions are exchanged for H^+ in the bulk structure of LLZO [Figure 2A][30].

Following heat treatment in the glovebox to remove carbonates, LLZO NFs were exposed to air with spectra taken after given time intervals. Even within a couple of minutes, the effects of carbonate formation are apparent. Figure 2B shows distortion and shifting of the cubic LLZO peaks as Li^+ is replaced with H^+ in the bulk structure. This process is most apparent in the Zr-O vibration at 640 cm^{-1} [Figure 2C], which not only blue-shifts but forms a shoulder at higher wavenumbers as well[31]. The reacted surface layer quickly accumulates Li_2CO_3, visible in Figure 2D. Interestingly, the accumulation of Li_2CO_3 seems to follow two distinct growth regimes [Figure 2E]: rapid growth in the first few hours of air exposure, followed by much slower but still continuous growth for up to a full day. Assuming a pseudo-first-order reaction, the kinetics for these growth regimes are 1.2×10^{-2} s^{-1} and 1.8×10^{-4} s^{-1}, respectively. This may be due to the blocking of surface sites by Li_2CO_3 to hinder reaction with H_2O and/or the ability of the LLZO lattice to accommodate H^+ and continue transporting Li^+ to the surface[32].

With the baseline LLZO response established, we examined the bulk LLZO lattice stability under certain conditions following silane treatment. For this study, we used a silane with terminal epoxide group (GPS)

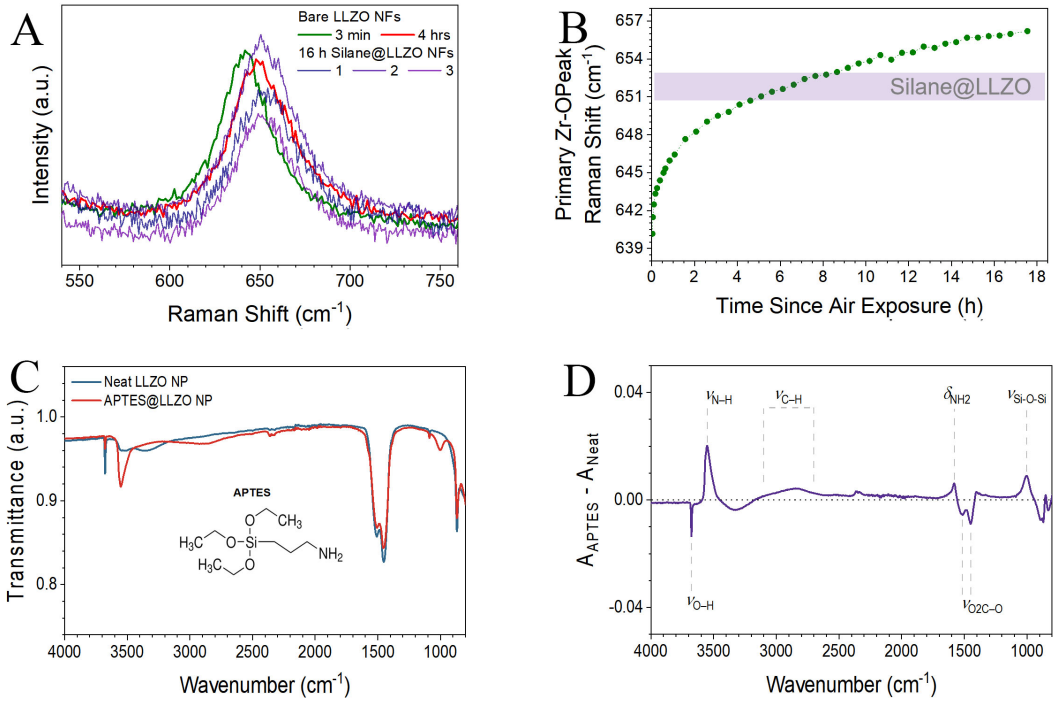

Figure 1. (A) Raman Zr-O peak in the LLZO nanofibers (B) Raman shift of Zr-O peak with air exposure time (C) FT-IR spectra of LLZO NP before (Neat LLZO NP) and after (APTES@LLZO NP) treatment with APTES (structure inset); (D) Differential absorbance spectra with APTES@LLZO NP subtracted from Neat LLZO NP. Positive values indicate new chemistries added to the material; negative values indicate chemistries removed from the material following silane treatment. LLZO: $Li_7La_3Zr_2O_{12}$; FT-IR: Fourier transform infrared spectroscopy; NPs: Nanoparticles; APTES: (3-aminopropyl)triethoxysilane.

instead of APTES to prevent the silane from acting as a proton source or pH buffer, but the results should be generally applicable to many silane chemistries. Figure 2F shows the Zr-O band of LLZO NFs after 16 h of direct air exposure and after 16 h of reaction with GPS under anhydrous conditions. While there is still a shift in the Zr-O band (~9 cm^{-1} blue-shift) indicative of some H^+/Li^+ exchange, there is much less than with unmodified LLZO exposed to air (~13 cm^{-1} blue-shift). After silane treatment, exposure to air for several hours does not lead to any further shift of the peak, indicating the surface is passivated by the silane and any residual Li_2CO_3.

Another benefit of the anhydrous silane treatment is limiting LLZO lattice disruption during the reaction itself. Most silane treatments involve acidic, partially aqueous solutions to activate the silane chemistry and undergo quick reactions with the oxide surface[16] However, as pointed out above, this is highly detrimental to LLZO. Figure 2G compares the Zr-O shift after GPS silane treatment and air exposure where the reaction was performed in anhydrous toluene or under an acidified methanol solution. The Zr-O blue-shift is significant (~19 cm^{-1}) and almost appears as two or three separate peaks for the acidic condition, indicating the extensive H^+/Li^+ exchange in the LLZO. This H^+ replacement of Li^+ is known to lower conductivity of bulk LLZO[33,34] so it seems necessary to limit this as much as possible by processing in aprotic solvents[34] to achieve optimal conductivity in LLZO-containing CPEs.

Conductivity of modified LLZO composites

To understand the effect of LLZO surface chemistry on Li^+ transport, we fabricated CPEs with 0, 10, and 50 wt % LLZO NPs. The LLZO was either unmodified ("Neat"), modified with APTES via anhydrous toluene reaction ("APTES@LLZO NP"), or coated with ~10 nm of Al_2O_3 via ALD ("Al_2O_3@LLZO NP"), as shown in

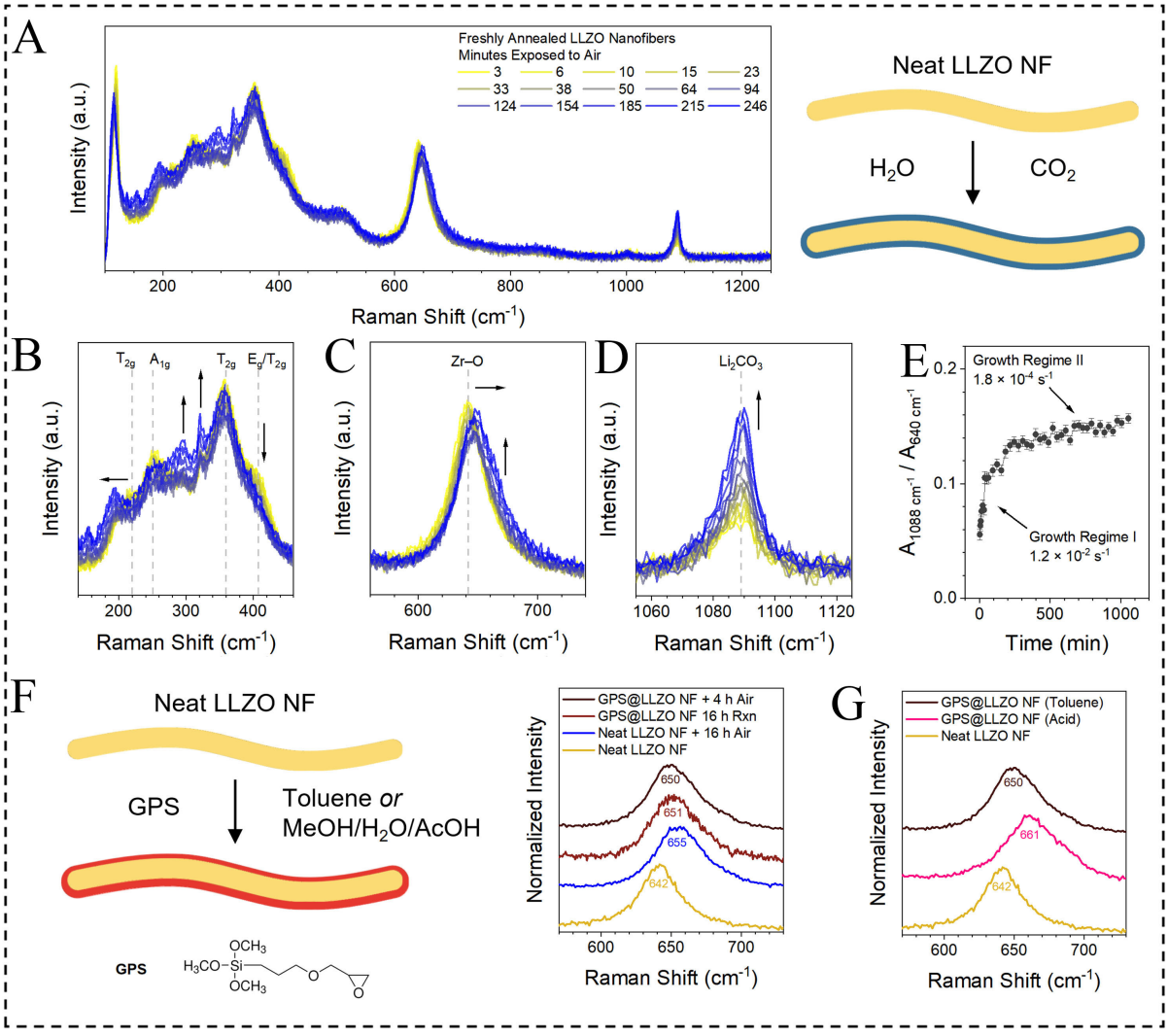

Figure 2. (A) Raman spectra of freshly annealed LLZO nanofibers from 3 to 246 min of air exposure as depicted on the right; (B-D) Detailed spectra showing peak shifts and intensity changes for (B) LLZO lattice vibrations; (C) Zr-O vibrations; and (D) C-O vibrations in Li_2CO_3; (E) Normalized integration of the Li_2CO_3 peak over time. Kinetics are estimated for pseudo-first-order reactions; (F) Spectra of the Zr-O band for LLZO NFs before and after 16 h of air exposure as well as 16 h of anhydrous treatment with GPS followed by 4 h of air exposure; (G) Comparison of the Zr-O band of freshly annealed LLZO NFs and LLZO NFs treated with GPS under acidified aqueous methanol and anhydrous toluene conditions. Raman shifts of the peak centers are labeled. LLZO: $Li_7La_3Zr_2O_{12}$; NFs: Nanofibers; GPS: Silane with terminal epoxide group.

Figure 3A. In our previous work, we demonstrated that ~10 nm Al_2O_3@Cu electrodes have R_{Int} values exceeding 10 kΩ cm², indicating that these layers have very slow ion transport, as R_{Int} reflects the conductivity of ions (i.e., Li^+) through the electrolyte-surface layers-electrode interfaces. Note that APTES acted as a model silane agent because it exhibits a slightly higher Li transference number compared to GPS-modified LLZO [Supplementary Figure 2]. Each of these represents control, positive, and negative conditions for how the LLZO surface hypothetically interacts with the surrounding polymer matrix without changing the particle morphology - covalently linking a polar organic linker to the surface should increase interaction with PEO more than the bare LLZO ceramic, while passivating the surface with a thick Al_2O_3 layer prevents any Li^+ exchange between the two phases.

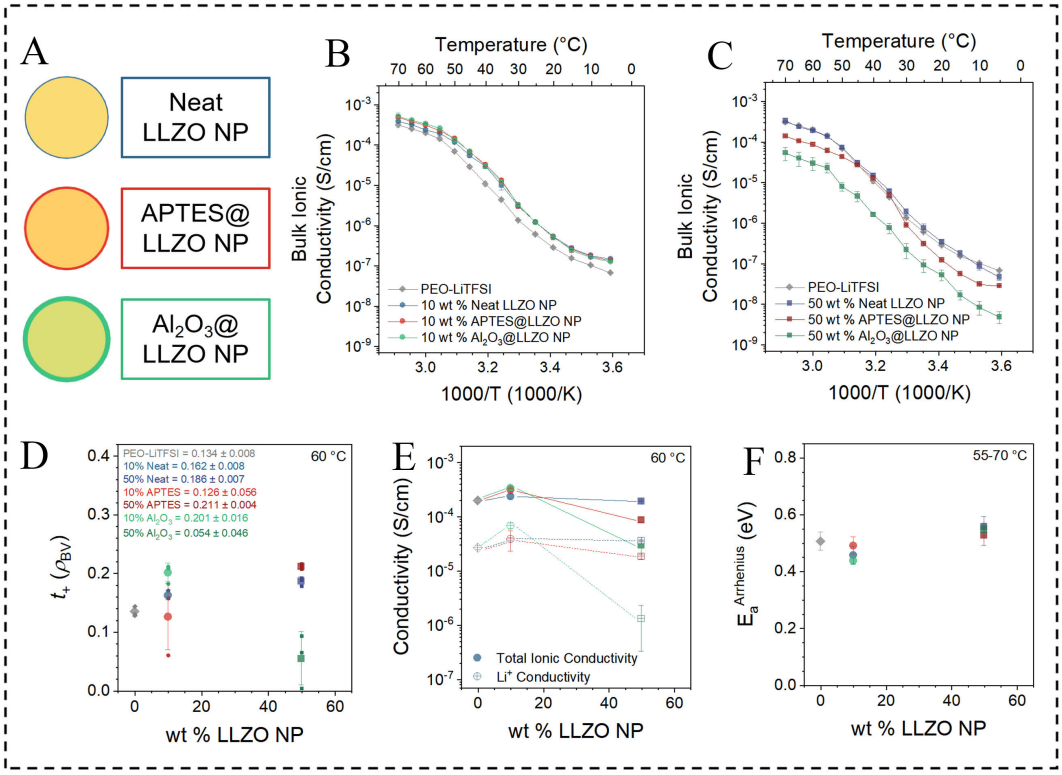

Figure 3. (A) Color scheme for modified LLZO nanoparticles; (B and C) Arrhenius-type plots of total bulk ionic conductivity for (B) 10 wt % and (C) 50 wt % LLZO NPs compared to PEO-LiTFSI (0 wt %); (D) Estimated transference numbers for all CPEs, quantified by the Bruce-Vincent current fraction ρ_{BV}. Small points represent values calculated from individual cells, and large points and error bars represent the mean and standard deviation of three cells; (E) Total ionic and Li^+ conductivities as a function of LLZO NP content; (F) Apparent Arrhenius activation energies for all CPEs at temperatures above the melting point of PEO. LLZO: $Li_7La_3Zr_2O_{12}$; NPs: Nanoparticles; APTES: (3-aminopropyl)triethoxysilane; PEO-LiTFSI: Poly (ethylene oxide)-lithium bis(trifluoromethanesulfonyl)imide; CPEs: Composite polymer electrolytes.

At 10 wt % LLZO NPs, the total bulk ionic conductivities of Neat, APTES, and Al_2O_3 samples are incredibly similar and greater than that of PEO-LiTFSI alone at all temperatures [Figure 3B]. However, at 50 wt % LLZO NPs, the conductivities vary drastically. Neat LLZO is fairly similar to PEO-LiTFSI; APTES@LLZO demonstrates lower conductivity at most temperatures but with different temperature dependencies, and Al_2O_3@LLZO shows conductivities more than order of magnitude lower than all other samples [Figure 3C]. Clearly, surface chemistry has a greater effect at higher fractional contents in the composites. Note that in Figure 3, by Neat LLZO, the authors indicate CPEs where the surface of the LLZO ceramic NPs are not modified in any fashion.

The temperature-dependent ionic conductivities of different CPEs plotted in Figure 3B and C demonstrate a reverse "S"-type shape. The reported ionic conductivity values are very well within the range reported in existing literature, within 10^{-8} - 10^{-3} S/cm[35] The flat region, with lower activation energy at higher temperatures (T > 55 °C), can be associated with faster ionic transport through the CPE with molten PEO. The higher activation energy observed at the intermediate temperatures (55 °C > T > 20 °C) can be attributed to the transport of the ionic species through the crystalline or semicrystalline PEO that demonstrates lower conductivity. The source of lower activation energy at lower temperatures (T < 20 °C) is unknown and can possibly be attributed to the variation in temperature dependence of ionic conductivity, which can be associated with the non-linear Vogel-Tammann-Fulcher (VTF) behavior. Note that transport

of the lithium ions, which is considered to be the major ion-carrying species, is assumed to occur through the bulk of the PEO or PEO/LLZO interface, and not through the bulk of LLZO.

These numbers represent the total ionic conductivity, including contributions from both Li^+ and the counterion $TFSI^-$. To probe true Li^+ transport, t_{Li+} values were estimated with the Bruce-Vincent method as current fractions (ρ_{BV}; see Supplementary Figures 3 and 4)[25]. We note that this method - which is predicated on a homogeneous polymer system - is likely not applicable to truly quantify transference numbers for heterogenous composite electrolytes with highly variable impedances[36]. Nonetheless, we expect that the qualitative trends here are still relevant based on the propensity of the electrolytes to achieve steady-state current-voltage profiles[37] [Supplementary Figure 5] with triplicate measurements, even if the exact t_{Li+} values may not be accurate. Figure 3D shows that adding 10 wt % LLZO NPs with any surface modification increases t_{Li+} above that of PEO-LiTFSI, from ~0.13 to ~0.16 for Neat LLZO and APTES@LLZO (disregarding one outlier) and surprisingly to ~0.20 for Al_2O_3@LLZO. When moving to 50 wt %, the surface chemistries diverge in much the same way as in the case of bulk conductivity. APTES@LLZO exhibits the highest t_{Li+} at ~0.21; Neat LLZO is close at ~0.19, but Al_2O_3@LLZO plummets to ~0.05. This agrees with the hypothesis that increasing LLZO-PEO interactions via silane chemistry helps Li^+ transport, while coating with Al_2O_3 shuts down those interactions completely.

Figure 3E plots the total ionic conductivity and estimated Li^+ conductivity ($\sigma_{Li+} = t_{Li+} \times \sigma_{Total}$) as a function of LLZO NP content at 60 °C. At 10 wt % LLZO NPs, surface chemistry matters very little and increases in both total ionic conductivity and relative Li^+ mobility are observed. At 50 wt %, Neat LLZO shows the highest Li^+ conductivity, while APTES@LLZO shows similar σ_{Li+} to PEO-LiTFSI despite having lower total conductivity. Al_2O_3@LLZO NPs at 50 wt % show extremely poor Li^+ conductivity at the 10^{-6} S/cm level. Despite these differences in total and Li^+ conductivity, the apparent Arrhenius activation energy [Figure 3F] in the 55-70 °C range, above the melting point of PEO, does not vary significantly across all surface chemistries and LLZO weight fractions (all within the 0.44-0.56 eV range). This indicates that PEO still dominates ion transport in these systems, and that bulk LLZO is not directly involved in Li^+ transport.

PEO-LLZO interphase resistance

The lack of through-LLZO Li^+ transport (ion movement from the polymer phase into LLZO, through the bulk of the LLZO phase, and back into the polymer phase) is likely due to the high interfacial resistance between LLZO and the PEO-LiTFSI matrix[38], which has been hypothesized to come from the restricted polymer movement, local polymer crystallization, and space charge effects at the ceramic interface[9,12,13,39]. The fact that different Li^+ transport is observed for both APTES@LLZO and Al_2O_3@LLZO compared to Neat LLZO implies that surface modification affects this process in some way, effectively changing the interphase resistance. We use the term "interphase" here because cations and/or anions (lithium, lanthanum, zirconium, carbon, oxygen, hydrogen, fluorine, sulfur, or nitrogen) must interdiffuse between an ordered ceramic phase and a more disordered polymer phase, and there is evidence in the literature that LLZO reacts with the ether chains in PEO to form decomposition layers more akin to a solid electrolyte interphase[40].

To quantify this interphase resistance, trilayer cells consisting of a sintered LLZO pellet sandwiched between thin 10-15 μm PEO-LiTFSI layers with blocking electrodes were prepared [Figure 4A][24,41] The LLZO pellet was freshly annealed in an Ar-filled glovebox within 24 h of cell assembly to remove added resistance from surface contaminants. APTES@LLZO pellets were prepared by soaking the annealed pellet in a 3 wt % APTES solution inside the glovebox for five hours. From Nyquist plots alone, cells with APTES@LLZO pellets exhibit lower total impedance than those with Neat LLZO [Figure 4B and Supplementary Figure 6].

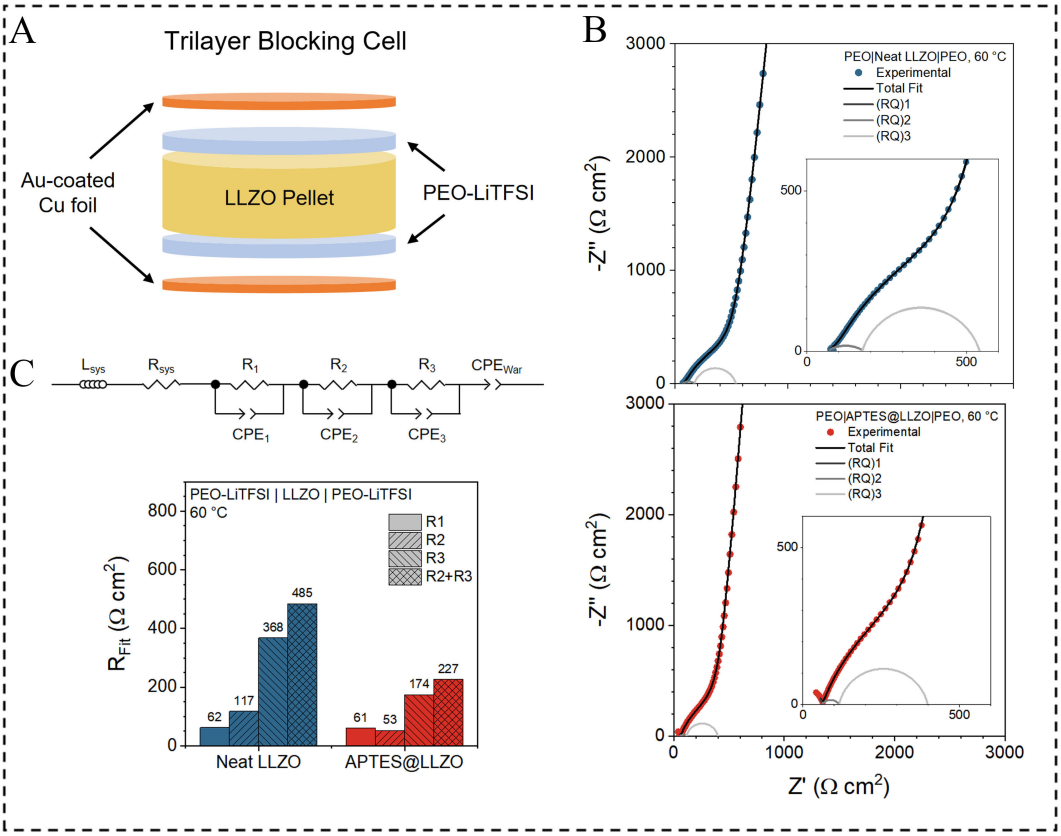

Figure 4. (A) Schematic of the trilayer blocking cells; (B) Nyquist plots of PEO-LiTFSI|LLZO|PEO-LiTFSI cells at 60 °C with Neat LLZO (top) and APTES@LLZO (bottom) pellets. Grayscale lines show semicircles from each fit R-CPE element; (C) Equivalent circuit and fit resistances of the cells at 60 °C. Measurements at 25 °C can be found in Supplementary Figure 6. LLZO: $Li_7La_3Zr_2O_{12}$; PEO-LiTFSI: Poly (ethylene oxide)-lithium bis(trifluoromethanesulfonyl)imide; APTES: (3-aminopropyl)triethoxysilane; CPEs: Composite polymer electrolytes.

Fitting to a three-part equivalent circuit provided the best fits and shows that while the bulk conductivities (R1) of both cells are identical, the resistances of the medium frequency R2 and R3 elements are halved when the LLZO is modified with APTES [Figure 4C][42,43]. These medium frequency elements are attributed to the LLZO|PEO-LiTFSI interphase resistance, as LLZO and PEO-LiTFSI alone are only expected to show one R-CPE element due to bulk transport[20]. We do not understand at this point why two semicircles are apparent (possibly due to resistance at the true microscopic LLZO|PEO interface followed by some longer-range resistance from the PEO domain, or due to imperfections in the LLZO pellet surface), but their combined resistance R2 + R3 is smaller with APTES modification regardless. The range of interfacial resistances observed in the trilayer analysis is around 200-500 W.cm^2, which resides within the range observed in other recent publications[44,45].

Lower interphase resistance for APTES@LLZO over Neat LLZO agrees with our observation of higher Li^+ current fractions, but the decrease in total conductivity at 50 wt % APTES@LLZO NPs as compared to Neat LLZO NPs (as reported in Figure 3E) cannot be explained from the observations made using the trilayer configuration. This trend of maximum conductivity boost at 5-20 wt % ceramic filler followed by lower conductivity at higher weight fractions[7,12] is theorized[39] but unexplained in the field according to the existing literature, which will be attempted in the next couple of paragraphs using a theoretical model.

To fit this unintuitive conductivity trend, a PEO-LiTFSI-LLZO NP composite model was constructed with two interphases between the bulk polymer matrix and the LLZO NP. The outer interphase is treated as conductive (i.e., conductivity in this phase is higher than bulk PEO-LiTFSI; dark blue in Figure 5A), while the inner interphase is treated as resistive (conductivity is lower than bulk PEO-LiTFSI; dark orange in Figure 5A). Presence of the resistive interphase adjacent to LLZO is based on the experimental evidence of a decrease in ionic conductivity in polymer electrolytes near a ceramic surface due to the impeded polymer chain motion[46]. The conductive interphase can be rationalized by the observation that adding nanofillers to semicrystalline polymers tends to decrease crystallinity[47,48], so a locally amorphous layer of PEO around the LLZO domain would experience increased conductivity relative to the semicrystalline bulk[49]. Interestingly, LLZO particles on the micron scale only decrease conductivity and do not show the local maximum at low weight fractions[7], indicating this plasticizing might be both material- and size-dependent and requires nanofillers[39]. The addition of this conductive interphase to a resistive interphase (already hypothesized theoretically[12]), where both interphases are dominated by the polymer, is a new conception that will be explored here. The interphase resistance between the resistive interphase and LLZO was treated as 4 kΩ cm^2 in all cases, but previous modeling has shown that even the hundreds of Ω cm^2 of the APTES@LLZO|PEO-LiTFSI interphase at 60 °C is still orders of magnitude greater than the 1-10 Ω cm^2 required to achieve Li^+ transport through the LLZO and not preferentially through the polymer phases[38].

From Figure 5A, it is clear that at low LLZO content (10 wt % LLZO is roughly equivalent to 4 vol % LLZO in PEO-LiTFSI composites), the volume fraction of the composite comprised of conductive interphases is relatively high. A Li^+ ion moving from one electrode to the other is likely to go through these regions, experiencing high mobility in the process. However, at high LLZO content, the volume fraction of resistive interphases takes over. In this case, there is essentially no pathway where ions can move without going through a resistive, low-mobility phase; or even if a percolating conductive phase exists, their volume fraction is usually very low and the pathway remains highly tortuous, which is unable to significantly contribute to the effective conduction of ions. The conductivities, thicknesses, and effective t_{Li+} of these layers - especially the inner resistive interphase - may be dependent on the particle surface chemistry, which changes how the PEO interacts at that boundary. Interphase conductivity and thickness were varied for Neat LLZO, APTES@LLZO, and Al_2O_3@LLZO composites to identify best fits at 25 °C and 60 °C, as were transference numbers to fit experimental data at 60 °C [Supplementary Tables 2 and 3]. The interphase thicknesses ranged from 200-400 nm for the inner resistive interphase (slightly larger than the 70-190 nm thicknesses predicted by Bonilla *et al.* for higher molecular weight PEO chains[12]), while the conductive interphase thickness ranged from 300-700 nm. Although this model treats the interphases as spatially distinct entities, in reality they should overlap to an extent due to the dynamic nature of the polymer phase. Also, considering the average size of the LLZO NPs being around 500 nm, the combined interphase regions with total thickness ranging between 500-950 nm substantially envelop the ceramic particles. Regardless, good fits between the model and experimental conductivity are seen in Figure 5B and C at low and high temperatures. Only incorporation of both conductive and resistive interphases allowed us to fit these trends, showing the complexity of the composite system.

It is worth pointing out that the mechanism of ion transport through the composite electrolyte is relatively simple, where the current is carried by the lithium cations (Li^+) and the salt anions ($TFSI^-$, used in the polymer electrolyte) through the migration and diffusion processes. At the interface between PEO and LLZO, evolution of the space charge layer is not considered[50], except for the presence of a large ohmic resistance that prevents transport of lithium ions from the polymer to the ceramic, and vice versa (for more details about the ion transport mechanisms and governing equations please see the Supplementary Information section). The experimentally observed increase and decrease in ionic conductivity with

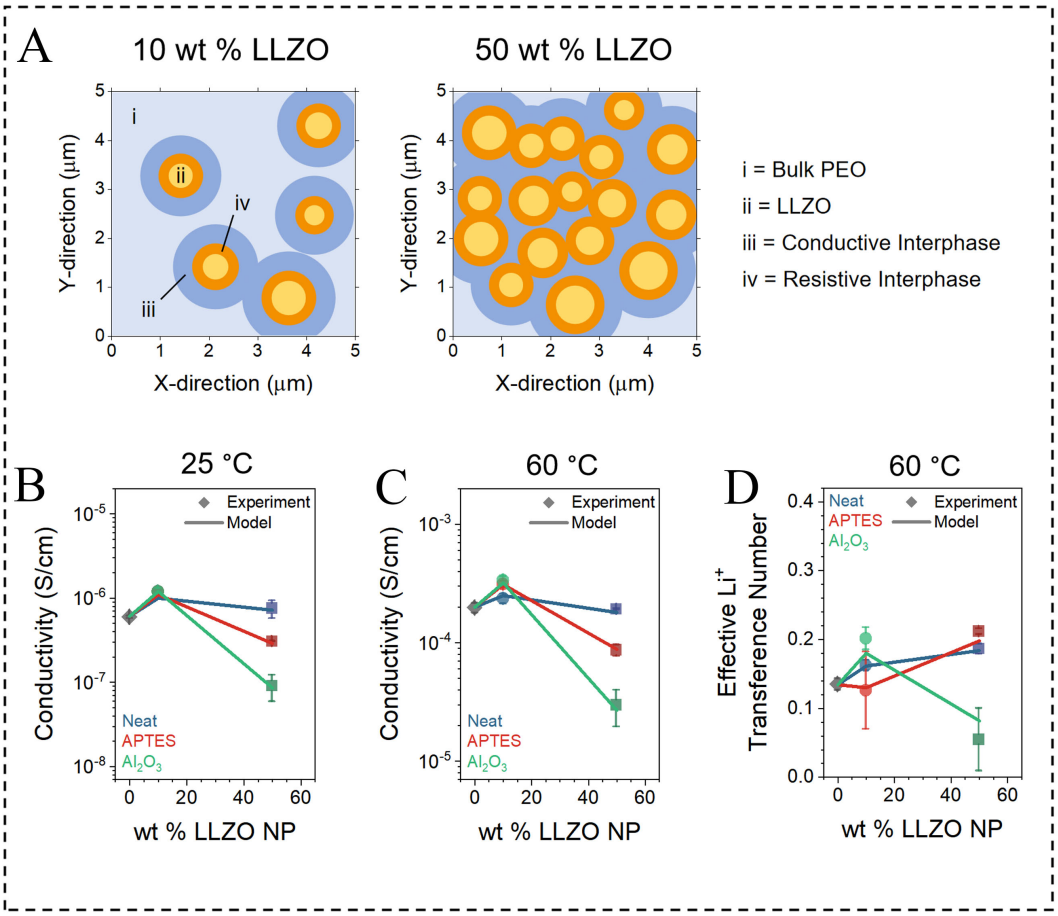

Figure 5. (A) Visualization of 10 wt % (4 vol %) and 50 wt % (20 vol %) LLZO NPs in a PEO-LiTFSI matrix. The bulk materials and interphases are labeled accordingly. Interphase resistances are not necessarily to scale; (B-D) Modeled values of LLZO NP composite electrolytes for (B) total ionic conductivity at 25 °C; (C) total ionic conductivity at 60 °C; and (D) effective bulk transference number at 60 °C overlaid with experimentally determined values. Fit parameters are found in Supplementary Table 1. LLZO: $Li_7La_3Zr_2O_{12}$; NPs: Nanoparticles; PEO-LiTFSI: Poly (ethylene oxide)-lithium bis(trifluoromethanesulfonyl)imide.

increasing ceramic fraction is captured by altering the properties of the polymer electrolyte located within a certain distance from the ceramic particles, which are characterized here as the resistive and conductive interphase regions. Ion transport mechanism within both the interphase layers constitutes migration and diffusion processes, which is very similar to the transport of ions within the bulk of PEO, but with different transport properties (such as conductivity, transference number, *etc.*). The flow of current within the composite electrolyte at room temperature and 60 °C is provided in Supplementary Figure 7 where it is clearly demonstrated that the majority of the current passes through the conductive interphase region.

The model is also able to replicate the macroscopic transference number by accounting for locally different transference numbers in the interphase regions [Figure 5D]. An effective bulk transference number was estimated from simulations and reflects a macroscopic value of microscopic interactions between bulk and interphase regions of differing transference numbers (t_{Li+}^{Bulk} and $t_{Li+}^{Interphase}$). While the bulk PEO-LiTFSI phase has similar transference numbers in all cases ($t_{Li+}^{Bulk} \sim 0.11\text{-}0.18$), the interphase controls effective Li^+ mobility, with APTES@LLZO showing $t_{Li+}^{Interphase} \sim 0.57$ and Al_2O_3@LLZO showing essentially $t_{Li+}^{Interphase} = 0$ [Supplementary Tables 2 and 3]. This interphase-dependent Li^+ mobility provides evidence for a surface-driven Li^+ transport mechanism and further evidence that Li^+ does not directly transport through

the LLZO bulk in these CPEs to any appreciable degree. The physical-chemical phenomena behind these changes are still an open question but could be related to surface segregation of anions or cations at particle surfaces due to the surface polarity or H-bonding in the case of silane chemistries, followed by differences in PEO chain conformation at larger length scales around the LLZO[12,39,51].

Chemistry and Li^+ transport at the LLZO|PEO-LiTFSI interphase

Solid-state Li NMR was used to investigate the chemistry of the LLZO|PEO-LiTFSI interphase and experimentally demonstrate how modification influences Li^+ transport at the interphase. Previous studies have used 2D NMR to measure Li^+ exchange between ceramic and polymer phases in composites[8,14,40,52-55] with some suggesting that secondary species such as LiOH on the LLZO surface mediate transport between these phases[14].

^{7}Li-^{7}Li 2D exchange spectroscopy (EXSY) was conducted on 50 wt % Neat LLZO NP and APTES@LLZO NP composite electrolytes [Figure 6A and B] cycled at low current densities. Two peak regions with peaks show Li^+ from the PEO-LiTFSI phase at -1.3 ppm and from LLZO phases at -0.6-1.0 ppm. The 2D NMR results show that for both Neat LLZO and APTES@LLZO composites, there is some overlap between both phases, indicating Li^+ exchange from PEO to LLZO and LLZO to PEO. This demonstrates that Li^+ is mobile to some extent through the composite interphase(s).

Notably, the LLZO region was very broad, with an upfield shoulder at -0.6 ppm discernable apart from the bulk LLZO signal at 0.1 ppm. This shoulder is typically attributed to the "LLZO-PEO interface"[40,52,53], something that is vaguely defined and which has been shown above to be very complicated from an electrochemical standpoint. To interrogate the chemistry of this "interphase", ^{7}Li-^{1}H cross-polarization magic-angle spinning NMR (CPMAS) was carried out on both Neat LLZO and APTES@LLZO composites. As seen in Supplementary Figure 8, excitation of the ^{1}H nuclei in the PEO phase only results in a signal from the ^{7}Li nuclei in the PEO-LiTFSI phase, not from the LLZO regions. Therefore, the chemistry of the "interphase" signal here is almost certainly LLZO-based. Whether this is a sub-population of non-bulk-like LLZO or a decomposed LLZO shell around the bulk LLZO particles[53] is still in question but appears to be influenced by the surface coating [Supplementary Figure 7]. This "LLZO interphase" is not necessarily the resistive interphase used in our modeling [Figure 5] but could contribute to the resistance against Li^+ transport through the bulk LLZO phase.

To better resolve and understand Li-dynamics in this interphase, 1D ^{6}Li NMR was employed on Neat LLZO NPs and APTES@LLZO NPs. First, we note a decrease in Li signal for APTES@LLZO NP in comparison with Neat LLZO NPs [Figure 6C]. These results are in great agreement with Inductively Coupled Plasma Optical Emission Spectrometry (ICP-OES) measurements [Supplementary Tables 2 and 3]. The chemical composition of APTES-modified LLZO shows slightly lower Li content (Li = 4.68) compared to the neat LLZO NP (Li = 5.99), indicating loss of Li during the surface modification and Li-vacancy formation. Furthermore, a significant decrease in the linewidth (full width at half maximum, FWHM) for the LLZO signal was observed [Figure 6C]. The peak for APTES@LLZO exhibits a FWHM of 46 Hz, approximately 30 Hz smaller than that of the Neat LLZO NP (72 Hz). Generally, a smaller linewidth indicates 'faster motion' of the nuclei, or greater rotational degrees of freedom. These observations together imply that the silane coating is modifying Li environment at the interface and causing the Li to move faster in the APTES@LLZO NP as opposed to the Neat LLZO NP. Given this, we expect that the interphase region between the silane coating and the LLZO will be Li^+ conductive and will allow for faster Li^+ transport than in Neat LLZO. This hypothesis is supported by the model that predicted higher conductivity of the resistive region for APTES@LLZO than Neat LLZO (see Supplementary Tables 2 and 3). To corroborate these

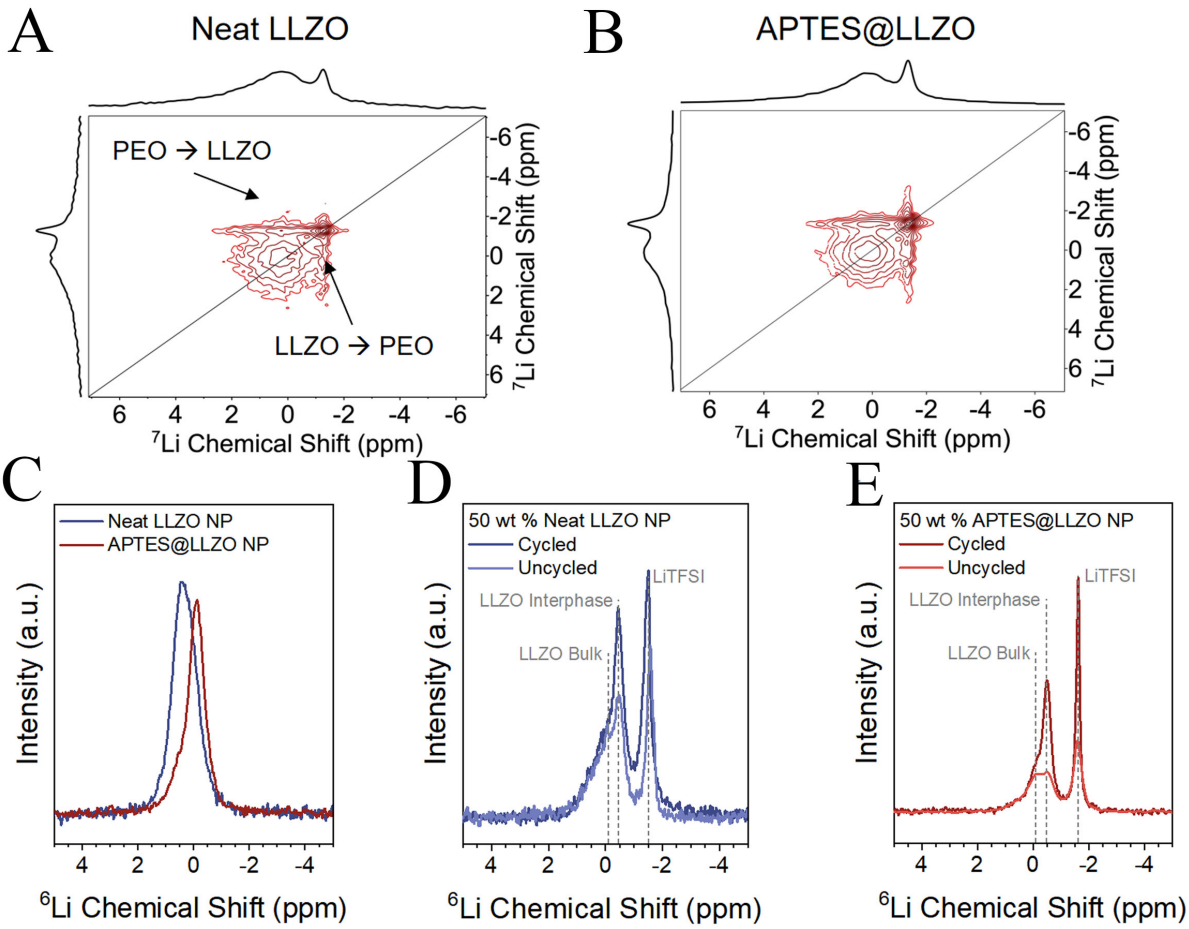

Figure 6. (A and B) ^{7}Li-^{7}Li 2D NMR spectra of (A) 50 wt % Neat LLZO NP and (B) 50 wt % APTES@LLZO NP composite membranes; (C) ^{7}Li-^{1}H CPMAS spectra showing Li$^+$-PEO interactions for both samples; (D and E) ^{6}Li NMR spectra of the composite samples before and after ^{6}Li||^{6}Li symmetric cell cycling. LLZO: $Li_7La_3Zr_2O_{12}$; NPs: Nanoparticles; NMR: Nuclear magnetic resonance; APTES: (3-aminopropyl)triethoxysilane; CPMAS: Cross-polarization magic-angle spinning; PEO: Poly (ethylene oxide).

findings, ^{6}Li NMR was used on composite membranes in the pristine form and after cycling with isotopically enriched ^{6}Li||^{6}Li symmetric cells. This allows an indirect view of where Li$^+$ moves in the cell during cycling by comparing the relative ^{6}Li amounts among PEO-LiTFSI, LLZO interphase, and bulk LLZO phases. Figure 6D and E shows ^{6}Li NMR spectra for 50 wt % Neat LLZO NP and APTES@LLZO NP composites before and after ^{6}Li enrichment through cycling. In both cases, the LiTFSI signal and LLZO interphase signal increase, while the bulk LLZO signal remains essentially unchanged. This confirms that Li$^+$ does not transport through the bulk of the LLZO particles, and apparently only moves through this interphase region. However, this interphase enrichment is more pronounced for APTES@LLZO than Neat LLZO, with a 52% relative increase in ^{6}Li signal with the APTES treatment *vs.* 13% relative increase without [Supplementary Figure 7]. This trend shows that APTES treatment can increase interfacial Li$^+$ transport in these LLZO-PEO composites.

Effects on cell characteristics and performance

With a fundamental understanding of how LLZO surface modification affects Li$^+$ transport in CPEs, we finally turned to Li||Li symmetric cell cycling to determine how modification affects cell performance. Nyquist plots of EIS for representative Neat LLZO NP, APTES@LLZO NP, and Al_2O_3@LLZO NP

composites are shown in Figure 7A. Despite having similar bulk resistance values with 10 wt % LLZO, the medium frequency impedance $R_{Anode\text{-}Int}$ (attributed to a combination of SEI resistance, charge transfer resistance, and other factors[56-58] at the electrolyte-Li anode interface) are surprisingly different. For Neat LLZO, the $R_{Anode\text{-}Int}$ decreases by half relative to PEO-LiTFSI; for APTES@LLZO, it is about the same; and for Al_2O_3@LLZO, it more than doubles. For 50 wt % LLZO, the $R_{Anode\text{-}Int}$ of Neat LLZO increases drastically above the 0 and 10 wt % cases; APTES@LLZO only increases slightly more than 10 wt %; and Al_2O_3 increases by an order of magnitude. These values better reflect the bulk conductivity trends of Figure 3, but there appear to be some hidden relationships between bulk Li^+ transport and interface impedance. Note that the charge transfer resistance at the Li|PEO-LiTFSI interface, measured at 60 °C, is around 300 Ω.cm², which is within the range reported by other recent publications that did not apply external pressure[59]. Lower resistances at the Li|PEO-LiTFSI interface can be obtained by either operating at higher temperatures[60], applying external pressure[61], or through the adoption of complex electrode/cell fabrication procedures[43].

Next, the Li||Li cells were galvanostatically cycled at increasing 10 μA/cm² intervals for ten minutes at a time, followed by extended rest periods, to determine the critical current density (CCD) at which the cell exhibits soft-shorts or complete short-circuiting [Figure 7B and Supplementary Figure 9][62]. This unidirectional, short pulse-long rest protocol was chosen to only allow time for voids in the stripped lithium working electrode to fill in and not lead to current focusing that would cause the cell to prematurely short[63]. We also chose short times to allow better comparison with the PEO-LiTFSI control condition, as previous work from our group with continual plating and stripping shows that the inclusion of ceramic fillers artificially increases the CCD by creating tortuous pathways for dendrite growth and breaking up lithium filaments before they short[10], a mechanism not possible with 0 wt % LLZO.

Figure 7C shows the CCD as a function of LLZO content for the three different LLZO surface modifications. The measured CCDs are in the range of 100 μA/cm² to 250 μA/cm² (or 0.1 mA/cm² to 0.25 mA/cm²), which are very well within the range of critical currents reported in the literature for PEO-based dry polymer electrolytes[64,65]. Surprisingly, none of the composites have significantly higher CCDs than PEO-LiTFSI alone, and many cells even short at lower current densities. This indicates that something other than transference number - the typical direct link to improved cycling performance - is controlling cell performance, as Figure 7C bears little resemblance to Figure 3D. To establish what controls CCD in these cells, linear regressions between CCD and total ionic conductivity, Li^+ conductivity, and $R_{Anode\text{-}Int}$ were performed [Figure 7D and E]. Surprisingly again, the correlation between σ_{Li+} and CCD is low (R^2~0.106), while the CCD correlations with σ_{Total} (R^2~0.645) and $R_{Anode\text{-}Int}$ (R^2~0.546) are stronger. Another interesting observation is that correlations are clear for high resistance data (low conductivity and high $R_{Anode\text{-}Int}$), but at low resistances, the correlations are less certain due to spread in the data. This makes sense if bulk mass transport ($\sigma_{Total/Li+}$) is the primary limiting factor if the conductivity is very low, but some other factor in the cell controls CCD even when the cell is not near the mass transport limit. Our observations of all the cells tested here show that $R_{Anode\text{-}Int}$ is usually a good indicator of how quickly a cell will short, as high interface resistance possibly leads to current focusing during Li plating, which quickly leads to filament formation and shorting.

The best correlation between all studied parameters [Supplementary Figure 10] is actually between $R_{Anode\text{-}Int}$ and σ_{Li+} (R^2~0.664), as seen in Figure 7F. In this way, σ_{Li+}, which is related to the Li^+ diffusivity - a true descriptor of limiting current of an electrolyte[66-68] - does influence the CCD. However, due to the practical issues associated with many electrochemical cell designs (uneven pressure in the cell stack, heterogeneous thickness of electrolytes, electrode roughness and purity, *etc.*) and the propensity of lithium metal to form uncontrolled filaments, Li^+ diffusivity only indirectly controls the measured performance limit of the cell.

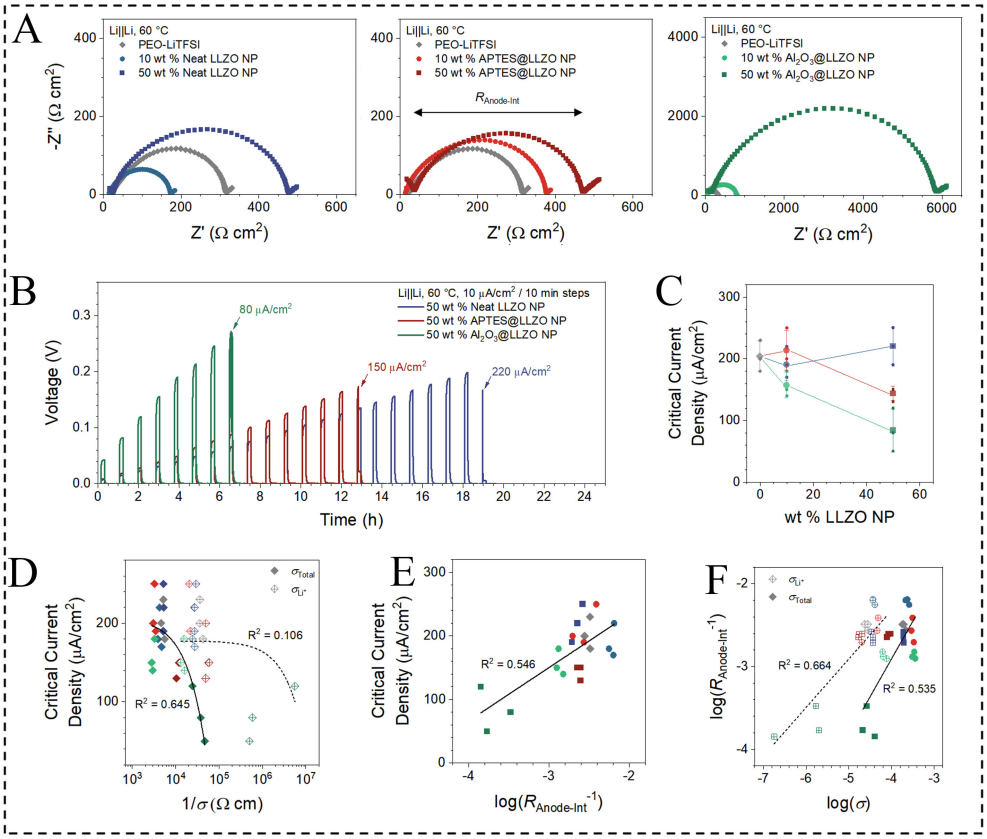

Figure 7. (A) Nyquist plots of representative Li||Li symmetric cells comparing PEO-LiTFSI with 10 and 50 wt % Neat LLZO NP (left), APTES@LLZO NP (middle), and Al_2O_3@LLZO NP composites; (B) Representative galvanostatic cycling curves (10 min applied current, 40 min rest) for 50 wt % LLZO NP composites with different surface modifications; (C) Critical current density as a function of LLZO content. Small points represent values measured from individual cells, and large points and error bars represent the mean and standard deviation of three cells; (D) Correlation between CCD and total ionic and Li^+ conductivities; (E) Correlation between CCD and $R_{Anode\text{-}Int}$; (F) Correlation between $R_{Anode\text{-}Int}$ and total ionic and Li^+ conductivities; All points in (D-F) are individual cells. Reported R^2 values are from linear regressions (solid and dashed lines) of the presented data. LLZO: $Li_7La_3Zr_2O_{12}$; NPs: Nanoparticles; PEO-LiTFSI: Poly (ethylene oxide)-lithium bis(trifluoromethanesulfonyl)imide; APTES: (3-aminopropyl)triethoxysilane; CCD: Critical current density.

Recent works have demonstrated ways to circumvent some of these challenges to probe performance even in coin cell formats[68,69].

In addition to these practical design improvements, we would like to draw the field's attention to the fundamental and intricate ways Li^+ transport as a bulk property can influence the behavior at interfaces within the battery [Figure 8]. Lithium-ion transport is not simply increased by adding Li-containing particles; as we have demonstrated, Li^+ does not move directly from the polymer through LLZO under these conditions due to large interfacial barriers. Multiple interfaces and interphases exist in an inherently heterogenous CPE. The interphases formed between ceramic particles and the polymer matrix dictate not only total ionic conductivity but also local conductivity of Li^+ around the particle surface. Depending on the volume fraction of the ceramic filler, as well as the surface chemistry that may help or hinder Li^+ mobility, the resulting size and conductivity of these interphases lead to global increases or decreases in Li^+ conductivity. At the electrode interface, Li^+ must move from the bulk electrolyte into the SEI, which is typically assumed to be a single-ion conductor made of inorganic and organic salt-like lithium compounds. Therefore, lithium-ion conductivity - a mixture of both transference number and total ionic conductivity - and not total conductivity dictates how quickly Li^+ cations can make it to the anode surface to

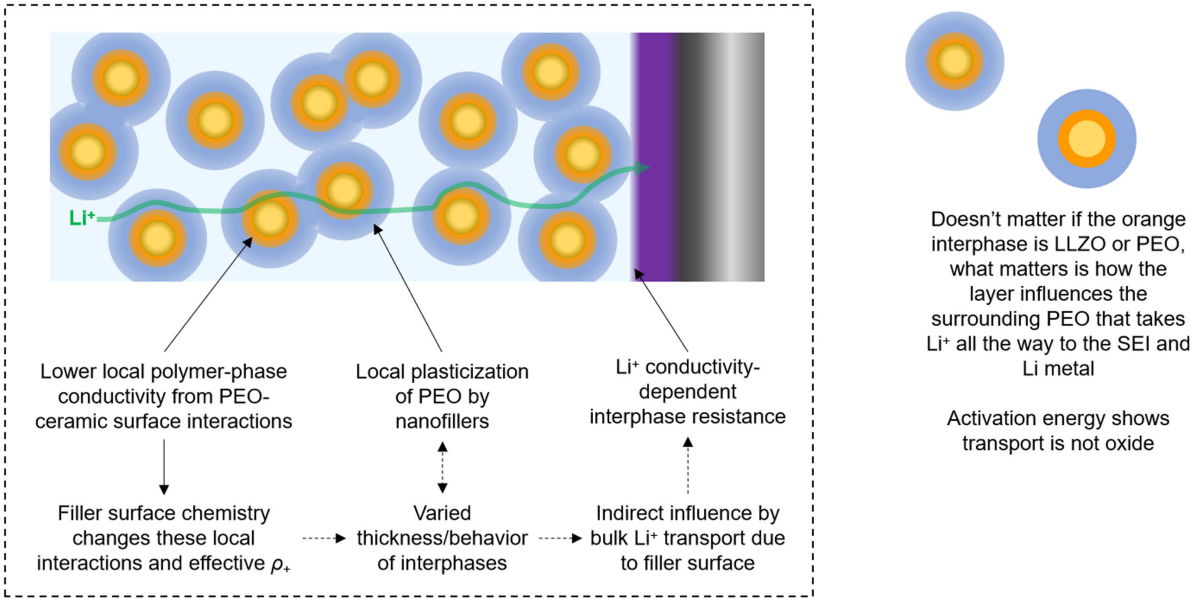

Figure 8. Schematic showing how local interphases in the bulk composite electrolyte can influence resistance at the electrode-electrolyte interface.

plate lithium, even if LLZO is not directly in or present at the SEI. In this way, "interface resistance" is not just a measure of how conductive the SEI is, but also how the bulk and the SEI interact. Since most lithium metal cells with composite electrolytes at the research level fail due to shorting from inhomogeneous lithium metal plating that is dependent on the SEI, it is important to determine how the fundamental, measurable properties of the cell - bulk, SEI, interface, and diffusion resistances - are linked to design better electrolytes moving forward.

CONCLUSIONS

We have demonstrated how surface modification of LLZO nanofillers in LLZO-PEO-LiTFSI composite electrolytes can improve or hinder overall conductivity and cell resistance by causing local changes in Li^+ transport. Functionalization of LLZO was carried out with an anhydrous silane treatment to prevent disruption of the bulk LLZO structure due to H^+/Li^+ exchange in ambient air. CPEs with 10 wt % Neat LLZO, APTES@LLZO, and Al_2O_3 NPs show virtually no difference in conductivity. At 50 wt % LLZO loading, APTES@LLZO has slightly decreased conductivity but slightly higher effective t_{Li+} than Neat LLZO, while Al_2O_3@LLZO decreases massively in conductivity and transference. Trilayer electrolyte experiments show that APTES functionalization decreases the apparent PEO-LLZO interphase resistance from 485 Ω cm^2 to 227 Ω cm^2 at 60 °C, which explains slightly better Li^+ transference but is still too high to truly achieve Li^+ transport through the PEO-LLZO interphase in composites. The non-linear trends in conductivity and transference number with LLZO weight fraction and surface chemistry are successfully analyzed with a two-interphase model: a resistive interphase at the immediate LLZO surface, and a conductive interphase surrounding this resulting from local PEO plasticization, which can be characterized as a major finding of this article.

Solid-state ^{7}Li NMR shows Li^+ exchange between LLZO and PEO phases with both Neat and APTES@LLZO NPs in 50 wt % LLZO composites. However, ^{6}Li exchange and CPMAS experiments show that only a "LLZO interphase" is enriched with ^{6}Li during cell cycling, and virtually no Li^+ transport occurs through the bulk of LLZO, in contrast to many claims in the literature. Appropriate characterization of the lithium

transport pathway through the LLZO/PEO composite electrolyte using NMR, providing strong evidence of possible lithium transport through the surface of LLZO, is another major finding reported in this article.

Connecting the different surface chemistries to CCD and anode interface resistance in Li||Li symmetric cells reveals subtle relationships between local Li^+ transport and macroscopic cell performance. A mechanism for how LLZO-PEO interphases in the bulk can influence electrode-electrolyte interface resistance is proposed based on these results. Given that increasing LLZO content hinders rather than increases Li^+ conductivity, Li^+ transport is highly sensitive to filler surface chemistry, and virtually no Li^+ flows through bulk LLZO phases during cell cycling as determined by NMR, the typically reported mechanism of rapid ion transport through active fillers in the composite electrolyte field is found to be dubious unless the electrolyte system is heavily modified. A surface-mediated, interfacial transport pathway better explains any transport enhancements in CPEs with active and inactive fillers in a polymer matrix. This work demonstrates that the hidden interfaces in inherently heterogenous CPEs can be effectively tuned but must be considered to understand performance of the entire solid-state battery.

DECLARATIONS

Authors' contributions

Planned experiment planning, conducted electrochemical experiments, analyzed data, and contributed to writing: Counihan, M. J.
Planned experiment planning, fabricated materials, characterized materials, analyzed data, and contributed to writing: Lee, J.
Conducted solid-state NMR experiments, analyzed data, and contributed to writing: Mirmira, P.
Performed computational modeling, analyzed data, and contributed to writing: Barai, P.
Fabricated materials and performed material characterization: Burns, M. E.
Interpreted data and supervised the project: Amanchukwu, C. V.
Interpreted data and supervised the project: Srinivasan, V.
Planned experiments, interpreted data, supervised the project, and contributed to writing: Zhang, Y.
Planned experiments, interpreted data, supervised the project, and contributed to writing: Tepavcevic, S.

Availability of data and materials

All data can be available upon an E-mail request to the corresponding author.

Financial support and sponsorship

This work was funded by the USA. Department of Energy, Office of Energy Efficiency and Renewable Energy Vehicle Technologies Program (Grant# VT1201000), with support from Thompson, S. T. and Duong, T. Research was carried out at Argonne National Laboratory which is supported by the USA. Department of Energy, Office of Science, Office of Basic Energy Sciences, under contract no. DE-AC02-06CH1135. Roll-to-roll electrospinning and slot-die coating capabilities were established with the funding support from the Roll-to-Roll Advanced Materials Manufacturing DOE Laboratory Collaboration program sponsored by the USA. Department of Energy, Office of Energy Efficiency and Renewable Energy Advanced Manufacturing Office (AMO). Use of the Center for Nanoscale Materials, an Office of Science user facility, was supported by the USA. Department of Energy, Office of Science, Office of Basic Energy Sciences, under Contract No. DE-AC02-06CH11357. Use of the Materials Engineering Research Facility (MERF) at Argonne National Laboratory was supported by the USA. Department of Energy. C.V.A. and P.M. acknowledge the UChicago Materials Research and Engineering Center (MRSEC), which is funded by the National Science Foundation under Award DMR-2011854. We thank Dr. Mane, A. for assisting with deposition of Al_2O_3 via ALD and Dr. Tsai, C. L. for providing LLZO pellet samples.

Conflicts of interest

All authors declared that there are no conflicts of interest.

Ethical approval and consent to participate

Not applicable.

Consent for publication

Not applicable.

REFERENCES

1. Grundish, N. S.; Goodenough, J. B.; Khani, H. Designing composite polymer electrolytes for all-solid-state lithium batteries. *Curr. Opin. Electrochem.* **2021**, *30*, 100828. DOI
2. Yao, P.; Yu, H.; Ding, Z.; et al. Review on polymer-based composite electrolytes for lithium batteries. *Front. Chem.* **2019**, *7*, 522. DOI PubMed PMC
3. Yu, X.; Manthiram, A. A review of composite polymer-ceramic electrolytes for lithium batteries. *Energy. Storage. Mater.* **2021**, *34*, 282-300. DOI
4. Meng, N.; Zhu, X.; Lian, F. Particles in composite polymer electrolyte for solid-state lithium batteries: a review. *Particuology* **2022**, *60*, 14-36. DOI
5. Bonnick, P.; Muldoon, J. The quest for the holy grail of solid-state lithium batteries. *Energy. Environ. Sci.* **2022**, *15*, 1840-60. DOI
6. Lu, X.; Wang, Y.; Xu, X.; Yan, B.; Wu, T.; Lu, L. Polymer-based solid-state electrolytes for high-energy-density lithium-ion batteries - review. *Adv. Energy. Mater.* **2023**, *13*, 2301746. DOI
7. Zagórski, J.; López, A. J. M.; Cordill, M. J.; Aguesse, F.; Buannic, L.; Llordés, A. Garnet-polymer composite electrolytes: new insights on local Li-ion dynamics and electrodeposition stability with Li metal anodes. *ACS. Appl. Energy. Mater.* **2019**, *2*, 1734-46. DOI
8. Yang, T.; Zheng, J.; Cheng, Q.; Hu, Y. Y.; Chan, C. K. Composite polymer electrolytes with $Li_7La_3Zr_2O_{12}$ garnet-type nanowires as ceramic fillers: mechanism of conductivity enhancement and role of doping and morphology. *ACS. Appl. Mater. Interfaces.* **2017**, *9*, 21773-80. DOI
9. Din, M. M. U.; Häusler, M.; Fischer, S. M.; et al. Role of filler content and morphology in LLZO/PEO membranes. *Front. Energy. Res.* **2021**, *9*, 711610. DOI
10. Counihan, M. J.; Powers, D. J.; Barai, P.; et al. Understanding the influence of $Li_7La_3Zr_2O_{12}$ nanofibers on critical current density and coulombic efficiency in composite polymer electrolytes. *ACS. Appl. Mater. Interfaces.* **2023**, *15*, 26047-59. DOI
11. Chan, C. K.; Yang, T.; Mark, W. J. Nanostructured garnet-type $Li_7La_3Zr_2O_{12}$: synthesis, properties, and opportunities as electrolytes for Li-ion batteries. *Electrochim. Acta.* **2017**, *253*, 268-80. DOI
12. Bonilla, M. R.; García, D. F. A.; Ranque, P.; Aguesse, F.; Carrasco, J.; Akhmatskaya, E. Unveiling interfacial Li-ion dynamics in $Li_7La_3Zr_2O_{12}$/PEO(LiTFSI) composite polymer-ceramic solid electrolytes for all-solid-state lithium batteries. *ACS. Appl. Mater. Interfaces.* **2021**, *13*, 30653-67. DOI PubMed
13. Brogioli, D.; Langer, F.; Kun, R.; La, M. F. Space-charge effects at the $Li_7La_3Zr_2O_{12}$/poly(ethylene oxide) interface. *ACS. Appl. Mater. Interfaces.* **2019**, *11*, 11999-2007. DOI PubMed
14. Ranque, P.; Zagórski, J.; Devaraj, S.; Aguesse, F.; López, A. J. M. Characterization of the interfacial Li-ion exchange process in a ceramic-polymer composite by solid state NMR. *J. Mater. Chem. A.* **2021**, *9*, 17812-20. DOI
15. Kondori, A.; Esmaeilirad, M.; Harzandi, A. M.; et al. A room temperature rechargeable Li_2O-based lithium-air battery enabled by a solid electrolyte. *Science* **2023**, *379*, 499-505. DOI
16. Yan, C.; Zhu, P.; Jia, H.; et al. Garnet-rich composite solid electrolytes for dendrite-free, high-rate, solid-state lithium-metal batteries. *Energy. Storage. Mater.* **2020**, *26*, 448-56. DOI
17. Kuhnert, E.; Ladenstein, L.; Jodlbauer, A.; et al. Lowering the interfacial resistance in $Li_{6.4}La_3Zr_{1.4}Ta_{0.6}O_{12}$|poly(ethylene oxide) composite electrolytes. *Cell. Rep. Phys. Sci.* **2020**, *1*, 100214. DOI
18. Hou, W.; Chen, Z.; Wang, S.; et al. A "concentrated ionogel-in-ceramic" silanization composite electrolyte with superior bulk conductivity and low interfacial resistance for quasi-solid-state Li metal batteries. *Energy. Environ. Mater.* **2024**, *7*, e12736. DOI
19. Helmers, L.; Frankenberg, F.; Brokmann, J.; et al. Functionalized thiophosphate and oxidic filler particles for hybrid solid electrolytes. *ChemElectroChem* **2023**, *10*, e202300310. DOI
20. Yu, D.; Tronstad, Z. C.; McCloskey, B. D. Lithium-ion transport and exchange between phases in a concentrated liquid electrolyte containing lithium-ion-conducting inorganic particles. *ACS. Energy. Lett.* **2024**, *9*, 1717-24. DOI PubMed PMC
21. Ihrig, M.; Finsterbusch, M.; Tsai, C.; et al. Low temperature sintering of fully inorganic all-solid-state batteries - impact of interfaces

on full cell performance. *J. Power. Sources.* **2021**, *482*, 228905. DOI

22. Cheng, L.; Liu, M.; Mehta, A.; et al. Garnet electrolyte surface degradation and recovery. *ACS. Appl. Energy. Mater.* **2018**, *1*, 7244-52. DOI
23. Larraz, G.; Orera, A.; Sanjuán, M. L. Cubic phases of garnet-type $Li_7La_3Zr_2O_{12}$: the role of hydration. *J. Mater. Chem. A.* **2013**, *1*, 11419. DOI
24. Gupta, A.; Sakamoto, J. Controlling ionic transport through the PEO-LiTFSI/LLZTO interface. *Electrochem. Soc. Interface.* **2019**, *28*, 63-9. DOI
25. Evans, J.; Vincent, C. A.; Bruce, P. G. Electrochemical measurement of transference numbers in polymer electrolytes. *Polymer* **1987**, *28*, 2324-8. DOI
26. Huo, H.; Chen, Y.; Zhao, N.; et al. In-situ formed Li_2CO_3-free garnet/Li interface by rapid acid treatment for dendrite-free solid-state batteries. *Nano. Energy.* **2019**, *61*, 119-25. DOI
27. Ruan, Y.; Lu, Y.; Huang, X.; et al. Acid induced conversion towards a robust and lithiophilic interface for Li-$Li_7La_3Zr_2O_{12}$ solid-state batteries. *J. Mater. Chem. A.* **2019**, *7*, 14565-74. DOI
28. Guo, Y.; Cheng, J.; Zeng, Z.; et al. Li_2CO_3: insights into its blocking effect on Li-ion transfer in garnet composite electrolytes. *ACS. Appl. Energy. Mater.* **2022**, *5*, 2853-61. DOI
29. Besli, M. M.; Usubelli, C.; Metzger, M.; et al. Effect of liquid electrolyte soaking on the interfacial resistance of $Li_7La_3Zr_2O_{12}$ for all-solid-state lithium batteries. *ACS. Appl. Mater. Interfaces.* **2020**, *12*, 20605-12. DOI
30. Liu, X.; Chen, Y.; Hood, Z. D.; et al. Elucidating the mobility of H^+ and Li^+ ions in $(Li_{6.25-x}H_xAl_{0.25})La_3Zr_2O_{12}$ *via* correlative neutron and electron spectroscopy. *Energy. Environ. Sci.* **2019**, *12*, 945-51. DOI
31. Orera, A.; Larraz, G.; Rodríguez-Velamazán, J. A.; Campo, J.; Sanjuán, M. L. Influence of Li^+ and H^+ distribution on the crystal structure of $Li_{7-x}H_xLa_3Zr_2O_{12}$ ($0 \le x \le 5$) garnets. *Inorg. Chem.* **2016**, *55*, 1324-32. DOI
32. Hiebl, C.; Young, D.; Wagner, R.; Wilkening, H. M. R.; Redhammer, G. J.; Rettenwander, D. Proton bulk diffusion in cubic $Li_7La_3Zr_2O_{12}$ garnets as probed by single X-ray diffraction. *J. Phys. Chem. C.* **2019**, *123*, 1094-8. DOI
33. Rosen, M.; Ye, R.; Mann, M.; et al. Controlling the lithium proton exchange of LLZO to enable reproducible processing and performance optimization. *J. Mater. Chem. A.* **2021**, *9*, 4831-40. DOI
34. Grissa, R.; Payandeh, S.; Heinz, M.; Battaglia, C. Impact of protonation on the electrochemical performance of $Li_7La_3Zr_2O_{12}$ garnets. *ACS. Appl. Mater. Interfaces.* **2021**, *13*, 14700-9. DOI PubMed
35. Zaman, W.; Hortance, N.; Dixit, M. B.; De, A. V.; Hatzell, K. B. Visualizing percolation and ion transport in hybrid solid electrolytes for Li-metal batteries. *J. Mater. Chem. A.* **2019**, *7*, 23914-21. DOI
36. Gao, K. W.; Fang, C.; Halat, D. M.; Mistry, A.; Newman, J.; Balsara, N. P. The transference number. *Energy. Environ. Mater.* **2022**, *5*, 366-9. DOI
37. Chintapalli, M.; Timachova, K.; Olson, K. R.; et al. Relationship between conductivity, ion diffusion, and transference number in perfluoropolyether electrolytes. *Macromolecules* **2016**, *49*, 3508-15. DOI
38. Kim, H.; Barai, P.; Chavan, K.; Srinivasan, V. Transport and mechanical behavior in PEO-LLZO composite electrolytes. *J. Solid. State. Electrochem.* **2022**, *26*, 2059-75. DOI
39. Dissanayake, M.; Jayathilaka, P.; Bokalawala, R.; Albinsson, I.; Mellander, B. Effect of concentration and grain size of alumina filler on the ionic conductivity enhancement of the $(PEO)_9LiCF_3SO_3$:Al_2O_3 composite polymer electrolyte. *J. Power. Sources.* **2003**, *119-121*, 409-14. DOI
40. Zheng, J.; Dang, H.; Feng, X.; Chien, P.; Hu, Y. Li-ion transport in a representative ceramic-polymer-plasticizer composite electrolyte: $Li_7La_3Zr_2O_{12}$-polyethylene oxide-tetraethylene glycol dimethyl ether. *J. Mater. Chem. A.* **2017**, *5*, 18457-63. DOI
41. Chen, X. C.; Liu, X.; Samuthira, P. A.; Lou, K.; Delnick, F. M.; Dudney, N. J. Determining and minimizing resistance for ion transport at the polymer/ceramic electrolyte interface. *ACS. Energy. Lett.* **2019**, *4*, 1080-5. DOI
42. Vadhva, P.; Hu, J.; Johnson, M. J.; et al. Electrochemical impedance spectroscopy for all-solid-state batteries: theory, methods and future outlook. *ChemElectroChem* **2021**, *8*, 1930-47. DOI
43. Isaac, J. A.; Mangani, L. R.; Devaux, D.; Bouchet, R. Electrochemical impedance spectroscopy of PEO-LATP model multilayers: ionic charge transport and transfer. *ACS. Appl. Mater. Interfaces.* **2022**, *14*, 13158-68. DOI PubMed PMC
44. Kremer, S.; Rekers, R.; Sigar, U.; et al. A simple method for the study of heteroionic interface impedances in solid electrolyte multilayer cells containing LLZO. *ACS. Appl. Mater. Interfaces.* **2024**, *16*, 44236-48. DOI
45. Tenhaeff, W. E.; Perry, K. A.; Dudney, N. J. Impedance characterization of Li ion transport at the interface between laminated ceramic and polymeric electrolytes. *J. Electrochem. Soc.* **2012**, *159*, A2118-23. DOI
46. Dong, B. X.; Bennington, P.; Kambe, Y.; et al. Nanothin film conductivity measurements reveal interfacial influence on ion transport in polymer electrolytes. *Mol. Syst. Des. Eng.* **2019**, *4*, 597-608. DOI
47. Wang, J.; Fan, L.; Du, Q.; Jiao, K. Lithium ion transport in solid polymer electrolyte filled with alumina nanoparticles. *Energy. Adv.* **2022**, *1*, 269-76. DOI
48. Eriksson, T.; Mindemark, J.; Yue, M.; Brandell, D. Effects of nanoparticle addition to poly(ε-caprolactone) electrolytes: crystallinity, conductivity and ambient temperature battery cycling. *Electrochim. Acta.* **2019**, *300*, 489-96. DOI
49. St-onge, V.; Cui, M.; Rochon, S.; Daigle, J.; Claverie, J. P. Reducing crystallinity in solid polymer electrolytes for lithium-metal batteries via statistical copolymerization. *Commun. Mater.* **2021**, *2*, 187. DOI
50. Li, Z.; Huang, H. M.; Zhu, J. K.; et al. Ionic conduction in composite polymer electrolytes: case of PEO:Ga-LLZO composites. *ACS.*

Appl. Mater. Interfaces. **2019**, *11*, 784-91. DOI

51. Jayathilaka, P.; Dissanayake, M.; Albinsson, I.; Mellander, B. Effect of nano-porous Al_2O_3 on thermal, dielectric and transport properties of the $(PEO)_9LiTFSI$ polymer electrolyte system. *Electrochim. Acta.* **2002**, *47*, 3257-68. DOI
52. Zheng, J.; Tang, M.; Hu, Y. Y. Lithium ion pathway within $Li_7La_3Zr_2O_{12}$-polyethylene oxide composite electrolytes. *Angew. Chem. Int. Ed.* **2016**, *55*, 12538-42. DOI
53. Zheng, J.; Hu, Y. Y. New insights into the compositional dependence of Li-ion transport in polymer-ceramic composite electrolytes. *ACS. Appl. Mater. Interfaces.* **2018**, *10*, 4113-20. DOI
54. Wu, N.; Chien, P. H.; Qian, Y.; et al. Enhanced surface interactions enable fast Li^+ conduction in oxide/polymer composite electrolyte. *Angew. Chem. Int. Ed.* **2020**, *59*, 4131-7. DOI
55. Mirmira, P.; Fuschi, C.; Gillett, W.; et al. Nonconductive polymers enable higher ionic conductivities and suppress reactivity in hybrid sulfide-polymer solid state electrolytes. *ACS. Appl. Energy. Mater.* **2022**, *5*, 8900-12. DOI
56. Eckhardt, J. K.; Klar, P. J.; Janek, J.; Heiliger, C. Interplay of dynamic constriction and interface morphology between reversible metal anode and solid electrolyte in solid state batteries. *ACS. Appl. Mater. Interfaces.* **2022**, *14*, 35545-54. DOI
57. Eckhardt, J. K.; Fuchs, T.; Burkhardt, S.; Klar, P. J.; Janek, J.; Heiliger, C. 3D impedance modeling of metal anodes in solid-state batteries-incompatibility of pore formation and constriction effect in physical-based 1D circuit models. *ACS. Appl. Mater. Interfaces.* **2022**, *14*, 42757-69. DOI PubMed
58. Eckhardt, J. K.; Kremer, S.; Fuchs, T.; et al. Influence of microstructure on the material properties of LLZO ceramics derived by impedance spectroscopy and brick layer model analysis. *ACS. Appl. Mater. Interfaces.* **2023**, *15*, 47260-77. DOI
59. Liu, K.; Zhang, R.; Sun, J.; Wu, M.; Zhao, T. Polyoxyethylene (PEO)|PEO-perovskite|PEO composite electrolyte for all-solid-state lithium metal batteries. *ACS. Appl. Mater. Interfaces.* **2019**, *11*, 46930-7. DOI PubMed
60. Kim, H.; Balsara, N. P.; Srinivasan, V. Continuum description of the role of negative transference numbers on ion motion in polymer electrolytes. *J. Electrochem. Soc.* **2020**, *167*, 110559. DOI
61. Roering, P.; Overhoff, G. M.; Liu, K. L.; Winter, M.; Brunklaus, G. External pressure in polymer-based lithium metal batteries: an often-neglected criterion when evaluating cycling performance? *ACS. Appl. Mater. Interfaces.* **2024**, *16*, 21932-42. DOI PubMed PMC
62. Counihan, M. J.; Chavan, K. S.; Barai, P.; et al. The phantom menace of dynamic soft-shorts in solid-state battery research. *Joule* **2024**, *8*, 64-90. DOI
63. Fuchs, T.; Haslam, C. G.; Richter, F. H.; Sakamoto, J.; Janek, J. Evaluating the use of critical current density tests of symmetric lithium transference cells with solid electrolytes. *Adv. Energy. Mater.* **2023**, *13*, 2302383. DOI
64. Li, Z.; Fu, J.; Zhou, X.; et al. Ionic conduction in polymer-based solid electrolytes. *Adv. Sci.* **2023**, *10*, e2201718. DOI
65. Harry, K. J.; Hallinan, D. T.; Parkinson, D. Y.; MacDowell, A. A.; Balsara, N. P. Detection of subsurface structures underneath dendrites formed on cycled lithium metal electrodes. *Nat. Mater.* **2014**, *13*, 69-73. DOI PubMed
66. Gribble, D. A.; Frenck, L.; Shah, D. B.; et al. Comparing experimental measurements of limiting current in polymer electrolytes with theoretical predictions. *J. Electrochem. Soc.* **2019**, *166*, A3228-34. DOI
67. Maslyn, J. A.; Frenck, L.; Veeraraghavan, V. D.; et al. Limiting current in nanostructured block copolymer electrolytes. *Macromolecules* **2021**, *54*, 4010-22. DOI
68. Lee, J.; Kim, S. Y.; Hoffman, Z. J.; Chen, G.; Balsara, N. P. Experimental platform for determining the maximum limiting current in a polymer electrolyte. *ACS. Energy. Lett.* **2024**, *9*, 1796-802. DOI
69. Soulen, C.; Lam, N.; Holoubek, J.; Liu, P. Bridging the gap between pouch and coin cell electrochemical performance in lithium metal batteries. *J. Electrochem. Soc.* **2024**, *171*, 020535. DOI